LLNL-JRNL-2002899

Lawrence Livermore National Laboratory

The influence of cooling rates on strain phase diagrams and domain structures of ferroelectric thin films: A case study of PbTiO3

B Wang

June 2025

Disclaimer

This work performed under the auspices of the U.S. Department of Energy by Lawrence Livermore National Laboratory under Contract DE-AC52-07NA27344.

The influence of cooling rates on strain phase diagrams and domain structures of ferroelectric thin films: A case study of $PbTiO_3$

Meng-Jun Zhou[1,*], Peng Zhang[1], Bo Wang[2,*], Di Yi[3], and Ce-Wen Nan[3]

[1]State Key Laboratory of Advanced Technology for Materials Synthesis and Processing, Center of Smart Materials and Devices, School of Materials Science and Engineering, Wuhan University of Technology, Wuhan, 430070, China

[2]Materials Science Division, Lawrence Livermore National Laboratory, Livermore, CA 94550, USA

[3]School of Materials Science and Engineering, State Key Lab of New Ceramics and Fine Processing, Tsinghua University, Beijing, 100084, China

Corresponding authors

E-mail addresses: zhoumj@whut.edu.cn (Meng-Jun Zhou), wang111@llnl.gov (Bo Wang).

Abstract

Strain engineering has been established as an effective approach to control phase equilibria, domain configurations, and functional properties of ferroelectric thin films. Temperature-strain phase diagrams have been used as powerful tools for providing insights into strain engineering. However, almost all existing phase diagrams established using the phase-field approach assume quenching conditions without considering actual cooling rates during the post-deposition annealing process of ferroelectric thin films. Within this work, we systematically investigate the influence of cooling rates on domain structures and the strain-phase diagram of ferroelectric thin films using phase-field simulations, taking $PbTiO_3$ thin films as a model system. We found that both the position of phase boundaries in the strain phase diagrams and the domain morphology are significantly influenced by the cooling rates. It is revealed that while the paraelectric-ferroelectric phase boundary remains invariant, the phase boundaries between single-phase and multi-phase regions tend to shift toward the corresponding multi-phase region as the cool rate reduces. Slow cooling generally leads to more ordered domain structures with increased domain size. Using the obtained equilibrium domain structures, we calculated effective thermal conductivities and found significant variations that can be tuned by the cooling rates. This work reveals an underexplored yet critical impact of cooling rates on phase equilibria and domain structures in ferroelectric thin films, which may inspire further fine-tuning of domains and domain walls in low-dimensional ferroelectrics for multifunctional applications.

Keywords: Ferroelectric thin films; Domain structures; Phase diagrams; Phase-field simulation; Thermal conductivity

1. Introduction

Ferroelectric thin films have garnered significant theoretical and experimental research interest due to their exceptional functional properties, including remnant polarization [1], piezoelectric [2], dielectric [3], pyroelectric [4], electro-optic [5], and nonlinear optical properties [6]. These properties are influenced not only by the intrinsic lattice structures of ferroelectric phases but also by the types and spatial arrangements of ferroelectric domains [7–11].

Strain engineering has emerged as an effective method to control the domain structures of ferroelectric thin films [12–15]. Biaxial strains up to a few percentages can be imposed on the film through epitaxial growth on different substrates. The temperature-strain phase diagrams play a crucial role in the rational design of ferroelectric thin films through strain engineering [16–18]. These diagrams can be established using various computational methods, including *ab initio* approaches [19,20], thermodynamic modeling [21–28], and phase-field modeling [29–31]. While strain phase diagrams based on *ab initio* or thermodynamic approaches often assume homogeneous single-domain or simple multi-domain states, they neglect factors such as heterogeneous strains, electrical interactions, and domain wall contributions [19–28]. In contrast, phase diagrams obtained through phase-field simulations can account for these factors, providing better interpretations of experimental observations and enabling the theory-guided discovery of novel domain structures [29–31].

However, most existing phase diagrams of ferroelectric thin films established using the phase-field approach are determined by simulations of equilibrium domain structures under quenching conditions, where the temperature remains constant during domain formation. In experimental settings, ferroelectric thin films deposited at high temperatures typically cool down to room temperature at a finite rate [32]. It is well-established that cooling rates influence the position of phase boundaries in temperature-composition phase diagrams and the solid-state microstructures of metallic alloys [33,34]. This raises an important question: Do cooling rates similarly affect the temperature-strain phase diagram of ferroelectric thin films, particularly in terms of phase boundaries and equilibrium domain structures? This study aims to address this fundamental question and explore its implications for the design of ferroelectric thin films.

To address this question, we computationally establish the temperature-strain phase diagram of biaxially strained $PbTiO_3$ (PTO) at various cooling rates using the phase-field approach. For each cooling rate, we track the evolution of volume fractions of phases and domain variants during cooling to accurately determine phase boundary positions and obtain equilibrium domain structures at room temperature. Our findings reveal that while the phase boundary between paraelectric and ferroelectric phases remains invariant to cooling rates, some boundaries between single-phase and multi-phase regions shift depending on the cooling rates. Furthermore, the domain size, domain wall density, and volume fraction of domain variants in the equilibrium domain structure at room temperature are influenced by cooling rates. To understand these findings, we designed various regular domain patterns as initial states and analyzed their evolution during cooling using phase-field simulations. Notably, we discovered that certain exotic domain structures form only at specific cooling rates, aligning with experimental observations. Additionally, through effective property calculations, we demonstrate that altering cooling rates can significantly change domain wall density, thereby allowing substantial tuning of the thermal conductivity in PTO thin films. This study provides crucial insights into the role of cooling rates in determining the phase diagram and domain structures of ferroelectric thin films, offering new avenues for tailoring their properties through controlled cooling processes.

The rest of the article is organized as follows. In the Method section, we describe the phase-field approach of PTO thin films to establish the strain phase diagrams, emphasizing how cooling rate effects are incorporated and how phase boundary positions are determined. The Results section presents the temperature-misfit strain and room-temperature misfit strain-misfit strain phase diagrams of PTO films, derived from phase-field simulations at various cooling rates. In the Discussion, we propose a mechanism to explain why cooling rates only alter certain phase boundaries and how they influence equilibrium domain structure features. We also compare our theoretical predictions with experimental observations from the literature. Furthermore, we utilize the obtained domain structures and effective property calculations to demonstrate how the apparent thermal conductivity of PTO films can be tuned by manipulating domain

wall densities through cooling rates control. Finally, we summarize our findings and discuss their implications for computational and experimental research in ferroelectric materials.

2. Methods

In this work, we employed the phase-field method of ferroelectric thin films, using the spontaneous polarization $\boldsymbol{P} = (P_1, P_2, P_3)$ as the order parameter. And the evolution of which is governed by the time-dependent Ginzburg-Landau (TDGL) equation [35]:

$$\frac{\partial P_i(x,t)}{\partial t} = -L\frac{\delta F}{\delta P_i(x,t)}(i = 1,2,3), \tag{1}$$

where L and F represent the kinetic coefficient and the total free energy density of the system, respectively. The total free energy density F for the film consists of Landau free energy density f_{bulk}, gradient free energy density f_{grad}, electric free energy density f_{elec}, and elastic free energy density f_{elas}, which can be obtained using the following equation [35]:

$$F = \int_V (f_{\text{bulk}} + f_{\text{elas}} + f_{\text{elec}} + f_{\text{grad}})dV, \tag{2}$$

the detailed expression for f_{bulk}, f_{elas}, f_{elec}, and f_{grad} can be found in [35].

This study focuses on (001)-oriented PTO thin films, whose Landau coefficients, gradient energy coefficients, elastic stiffness tensor, and electrostrictive tensor can be found in the literature [30]. In the simulation, the system dimensions of the PTO thin films are $128\Delta x \times 128\Delta y \times 36\Delta z$, where $\Delta x = \Delta y = \Delta z = 1$ nm. The PTO thin film, substrate, and air layer have thicknesses of 20 nm, 12 nm, and 4 nm, respectively. In our simulations, the strain is assumed to remain constant during the cooling process, thereby neglecting the strain variation that may arise due to the mismatch in thermal expansion coefficients between the substrate and the film [36]. Additionally, the system is treated as isothermal, with a uniform temperature field throughout the simulation. The stable domain configurations in our work are obtained through the solution of the TDGL equation, starting from an initial polarization noise state and relaxed for a

sufficient time [16,18,37,38], except for those in Fig. 6, which are initialized from a preset domain structure. These simulated equilibrium domain structures can be used to determine the different phase regions in the phase diagrams by analyzing the volume fractions of each domain variant in the domain configurations. If the volume fraction of a primary domain variant exceeds 80%, it is considered a single-phase region. In multiphase regions, phase coexistence is defined by the volume fraction of the minor phase, with a 20% threshold based on our previous work [18]. For instance, if a simulated domain structure contains more than 20% of the a_1-phase in addition to the dominant *c*-phase, it is classified as a coexisting state of the a_1+*c*-phases.

In our work, the relationship between the simulation time step (Δt) and real time (in ps) has the following expression [39]:

$$\Delta t = \frac{m}{\alpha_0 L}, \tag{3}$$

where m controls the size of the marching step, and we typically set $m = 0.01$. Here α_0 denotes the absolute value of α_1 at 25°C, with α_1 being a Landau coefficient [30], expressed as $\alpha_0 = |\alpha_1|_{t=25°C} = 1.7252\times10^8$ $C^{-2}m^2N$, $L = 58$ $s^{-1}m^{-2}C^2N^{-1}$ represents the dimensionless kinetic coefficient governing domain mobility. Using this expression, the simulation time step (Δt) corresponds to 1 ps.

In this study, we simulate the four cooling rates (quenching, 0.18 K/ps, 0.06 K/ps, and 0.03 K/ps) in our work using the following method: For quenching, the system is instantaneously cooled from the initial polarization noise state to each given temperature and relaxed for a sufficient time, as shown in Fig. 1. For the other three linear cooling processes, the system starts from an initial polarization noise state, and the temperature is uniformly decreased from a high-temperature state (above the Curie temperature (T_c)) to each given temperature at constant cooling rates of 0.18 K/ps, 0.06 K/ps, and 0.03 K/ps, followed by sufficient relaxation (Fig. 1).

3. Results

3.1 Temperature-misfit strain phase diagrams with different cooling rates

Firstly, we conduct phase-field simulations to determine equilibrium domain configurations in (001)-oriented PTO thin films across various temperatures (from 300

K to 1200 K), misfit strains (ranging from −1% to 1%), and four cooling rates from quenching (fastest cooling) to 0.03 K/ps. From these simulations, we construct temperature-strain phase diagrams under varying cooling rates, as shown in Fig. 2(a). Under quenching condition, there are mainly four different phase regions including the cubic paraelectric phase, c-phase, a_1+a_2+c-phase, and a_1+a_2-phase, which are consistent with the previous findings [30,40]. For the other three cases, with cooling rates of 0.18 K/ps, 0.06 K/ps, and 0.03 K/ps, the phase diagrams are morphologically similar to the quenched case. By further comparing the phase diagrams for the above four cooling rates, it can be found that the phase boundary between the c and a_1+a_2+c phase regions shifts significantly to the right as the cooling rates decrease, while the other three phase boundaries remain invariant, including the paraelectric-ferroelectric phase boundary and the a_1+a_2//a_1+a_2+c phase boundary. Here, '//' represents the phase boundary. This shift indicates a prominent change in the critical strain and temperature for the c to a_1+a_2+c phase transition, which underscores the critical role of cooling rates in phase transitions.

Additionally, cooling rates also influence the polarization configuration of equilibrium domain structures at different phase regions of the above temperature-misfit strain phase diagram in Fig. 2(a). To better show the configuration changes, we select four typical points from the phase diagrams at various cooling rates as examples and compare the morphology of the equilibrium domain configurations in Fig. 2(b-e). The corresponding strain and temperature for the four selected points are marked in Fig. 2(a). It can be observed that the equilibrium domain morphologies at room temperature evolve from irregular to ordered configurations as the cooling rates decrease, which are accompanied by an increase in domain width and domain area. This coarsening behavior of the domain structures with decreasing cooling rates is discussed in detail in section 4.2 (Fig. 7). It is worth noting that, as shown in Fig. 2(c), under the strain conditions ($\varepsilon_{11} = \varepsilon_{22} = -0.2\%$) near the phase boundary between c and a_1+a_2+c phase regions, a reduction in cooling rates induces a phase transformation, from a mixed-phase (a_1+a_2+c) to a single-phase (c), which is consistent with the shift of corresponding phase boundary in Fig. 2(a). Furthermore, as illustrated in Fig. 2(d), under a different strain condition (ε_{11} = ε_{22} = 0.5%), the resulting a_1+a_2+c domain

configurations across varying cooling rates consist of coexisting a+c and a_1+a_2 domain regions, in agreement with prior experimental observations [38].

To quantify this phase transition behavior under different cooling rates, we track the evolution of volume fractions of c domains and a domains (V_f^c and V_f^a) for the equilibrium domain configurations during the cooling process under different cooling rates with a misfit strain of $\varepsilon_{11} = \varepsilon_{22} = -0.2\%$. As shown in Fig. 3, the volume fraction curves of c domains (V_f^c) under three different cooling rates nearly overlap during the cooling process from the initial paraelectric state to the ferroelectric state, which indicates that the cooling rates have a minor effect on the Curie temperature (T_c). However, the transition temperature from the c domains to the a_1+a_2+c domains is highly sensitive to the cooling rates. For instance, when cooling at a rate of 0.18 K/ps, the a domains first emerge around 600 K, whereas a slower rate of 0.06 K/ps delays their appearance to approximately 450 K. In contrast, under the slowest cooling rate of 0.03 K/ps, the c domains always remain stable until room temperature without forming any a domains. The difference in phase transition temperature between c domains and a domains induced by cooling rates is primarily attributed to the variation in the density of charged domain walls. A more detailed analysis of this mechanism is provided in section 4.1.

3.2 Misfit strain-misfit strain phase diagrams with different cooling rates

When films are deposited on orthogonal substrates, the lattice mismatch between the substrate and the film induces anisotropic mismatch strain, which significantly influences the domain morphologies of ferroelectric thin films [18,30]. In this study, we investigate the effect of cooling rates on the misfit strain-misfit strain phase diagram. Similar to Fig. 2, we also establish the room-temperature misfit strain-misfit strain phase diagrams of PTO films, with the strain range from −5% to 5%. As shown in Fig. 4(a), the simulated phase diagrams under four cooling rates (quenching, 0.18 K/ps, 0.06 K/ps, 0.03 K/ps) consistently exhibit seven phase regions: a_1-phase, a_2-phase, c-phase, a_1+c-phase, a_2+c-phase, a_1+a_2-phase, and a_1+a_2+c-phase, in agreement with prior reports based on quenching assumptions [30]. Notably, when the cooling rates are

reduced from quenching to 0.03 K/ps, the three single-phase regions (a_1-phase, a_2-phase, and c-phase) expand significantly, leading to the corresponding phase boundaries between single-phase and two-phase regions shifting toward the two-phase regions. In contrast, boundaries between two-phase and triple-phase regions exhibit differentiated behavior: the boundaries of a_2+c//a_1+a_2+c and a_1+c//a_1+a_2+c migrate toward the triple-phase region (a_1+a_2+c), whereas the a_1+a_2//a_1+a_2+c phase boundary remains invariant.

Next, we compare domain configurations under four anisotropic strains at different cooling rates in Fig. 4(b-e). As the cooling rates decrease, the domain configurations transition from disordered to ordered states, consistent with the trend shown in Fig. 2(b-e). This trend qualitatively agrees with previous experimental observations [41]. Additionally, similar coarsening behavior induced by decreasing cooling rates is also observed under anisotropic strain conditions, with a detailed discussion provided in Section 4.2 (Fig. 7). Moreover, reducing the cooling rates causes the domain structure to transition from a mixed a_2+c-phase to a single a_2-phase under the strain of $\varepsilon_{11} = -3\%, \varepsilon_{22} = 3\%$. This transition verifies the shift of the a_2+c//a_2 phase boundary depicted in Fig. 4(a).

4. Discussion

4.1 The mechanism of the cooling rates-dependence of the strain phase diagrams

To explore the underlying mechanisms why cooling rates only alter certain phase boundaries, we systematically compare the temperature-dependent evolution of domain configurations during rapid (0.1 K/ps) and slow (0.01 K/ps) cooling processes under the strain conditions of the three representative phase boundaries, as shown in Fig. 5(a-f). The representative phase boundaries and their corresponding strain conditions are as follows: (i) c//a_1+a_2+c, (ii) a_1//a_1+c, and (iii) a_1+a_2//a_1+a_2+c, which correspond to strain conditions of ($\varepsilon_{11} = \varepsilon_{22} = -0.2\%$), ($\varepsilon_{11} = 3\%, \varepsilon_{22} = -3\%$), and ($\varepsilon_{11} = \varepsilon_{22} = 0.5\%$), respectively.

First, we examine the effect of cooling rates on the phase boundary (c//a_1+a_2+c). We analyze the evolution of domain structures with temperature under different cooling

rates for the corresponding strain conditions, as shown in Fig. 5(a-b). Under rapid cooling (0.1 K/ps), the initially formed *c* domains at high temperature are rich in charged domain walls. As the temperature decreases to the nucleation temperature of *a* domains, the *a* domain nuclei tend to form at the charged domain walls (dashed squares in Fig. 5(a)). Upon continued cooling, the *a* domains grow and eventually stabilize into an a_1+a_2+c domain configuration at room temperature. In contrast, such charged domain walls are not observed under the slower cooling rate (0.01 K/ps), and the *c* domain structure stabilizes at room temperature. This may be attributed to prolonged structural relaxation that eliminates the charged domain walls. A similar phenomenon is observed for another phase boundary (a_1//a_1+c), as illustrated in Fig. 5(c-d). Under rapid cooling (0.1 K/ps), the charged domain walls between a_1^+ and a_1^- domain variants provide nucleation sites for the growth of *c* domains (dashed squares in Fig. 5(c)). In contrast, no such phenomenon is observed under slow cooling (0.01 K/ps, Fig. 5(d)), and the *a* domain structure remains stable at room temperature. The above-mentioned comparison of domain evolution under different cooling rates demonstrates that reducing the cooling rates changes the equilibrium domain structure, leading to the shift of phase boundaries between single-phase and multi-phase regions. Next, as shown in Fig. 5(e-f), we investigate why the phase boundary (a_1+a_2//a_1+a_2+c) remains invariant under different cooling rates. Unlike the previous two cases, the a_1+a_2 domain structure exhibits higher complexity due to the coexistence of a_1^+, a_1^-, a_2^+, and a_2^- domain variants. Consequently, the charged domain walls cannot be eliminated through prolonged structural relaxation under the slow cooling rate. The remaining charged domain walls serve as nucleation sites (dashed squares in Fig. 5(e-f)), promoting the phase transition from a_1+a_2-phase to a_1+a_2+c-phase. Therefore, the cooling rates have a minor effect on the boundary between two multiphase regions (a_1+a_2+c and a_1+a_2). In Fig. 5, the non-equilibrium structures labeled “Before nucleation” and “After nucleation” contain charged domain walls. As no charge compensation mechanism is implemented in this study, these charged domain walls gradually transform into stable neutral domain walls during subsequent cooling and relaxation through promoting the

nucleation of new domains.

To better understand the reason why the charged domain wall can promote the formation of new domains, we design two types of simple domain structures as initial states and analyze their evolution (Fig. 6(a-f)), along with their corresponding energy density variations (Fig. 6(g-h)) during cooling, using phase-field simulations.

In Fig. 6(a-f), two distinct *c* domain configurations are designed as initial states for the simulations: one containing charged domain walls and the other lacking charged domain walls, both subjected to biaxial compressive strain ($\varepsilon_{11} = \varepsilon_{22} = -0.2\%$), and cooled at a rate of 0.1 K/ps to obtain the equilibrium domain configurations. Their corresponding domain evolution exhibits significant differences, as shown in Fig. 6(a-f). For the case with charged domain walls (Fig. 6(a-c)), the initially preset *c* domain configuration undergoes nucleation of *a* domains during the cooling process (Fig. 6(b)), eventually evolving into an a_1+a_2+*c* domain structure at room temperature (Fig. 6(c)). In contrast, for the case without charged domain walls (Fig. 6(d-f)), the initially preset *c* domain configuration remains stable until room temperature. Compared to the nucleation processes observed in more complex domain morphologies (Fig. 5(a-d)), the charged domain walls in this simple preset structure are more clearly observed to serve as preferential nucleation sites for the new *a* domains (Fig. 6(a-c)), providing direct evidence for the role of charged domain walls in regulating phase transitions.

We also investigate the intrinsic mechanism of charged domain walls in promoting new domains formation from an energy perspective. A detailed analysis of the energy density evolution and corresponding electrostatic energy density distributions for the above-mentioned preset domain morphologies is provided in Fig. 6(g-h). In Fig. 6(g), for the case with charged domain walls, the reduction in total free energy is dominated by electrostatic free energy density (f_{elec}) and Landau free energy density (f_{bulk}). And the reduction in Landau free energy density correlates with the temperature-dependent polarization enhancement, whereas that in electrostatic free energy density results from the transition of charged domain walls to a non-charged configuration through domain nucleation. However, in Fig. 6(h), for the case without charged domain walls, the

decrease in total free energy density is dominated by the Landau free energy density due to the absence of charged domain walls.

Additionally, the corresponding electrostatic free energy density mappings for both the preset and final stable structures in the two processes described above are shown in the insets of Fig. 6(g-h). For the case with charged domain walls, we compare the electrostatic free energy density mappings in the insets of Fig. 6(g). It can be observed that the electrostatic energy density is significantly high at charged domain walls, and markedly reduces after nucleation. Conversely, for the case without charged domain walls presented in the insets of Fig. 6(h), the electrostatic energy distribution remains unchanged, preserving the initial domain structure.

Based on the analysis in Figs. 5 and 6, it can be deduced that the shift in boundaries between single-phase and multiphase regions is attributed to the dependence of charged domain wall density on the cooling rates. This dependence arises because the high local electrostatic energy density at charged domain walls promotes the nucleation of new domain variants.

4.2 Cooling-rate dependence of domain size in a_1+a_2, a_1+c, c domain structures

To further describe the cooling-rate dependence of domain morphology, we investigate the variations in domain size of three representative domain configurations as a function of cooling rate. The representative domain configurations and their corresponding strain conditions are as follows: (i) a_1+a_2 domains (Fig. 7(a)), (ii) a_1+c domains (Fig. 7(b)), and (iii) c domains (Fig. 7(c)), which correspond to strain conditions of ($\varepsilon_{11} = \varepsilon_{22} = 1\%$), ($\varepsilon_{11} = 2\%, \varepsilon_{22} = -3\%$), and ($\varepsilon_{11} = \varepsilon_{22} = -1\%$), respectively. For the a_1+a_2 and a_1+c domain configurations shown in Fig. 7(a-b), the domain size is quantified by measuring the domain width (DW) of a pair of domains (e.g., a_1+a_2 or a_1+c domain pairs). On the other hand, for the c domain configuration shown in Fig. 7(c), the domain size is characterized by calculating the average domain area (DA) of c^+ domains. Fig. 7(d) reveals a clear inverse correlation between domain size (DW and DA) and cooling rate. This negative correlation is consistent with previous experimental observations [42,43]. Notably, the variation in domain size of

the *c* domain configuration with cooling rates is significantly more pronounced than that of the other two domain structures (a_1+a_2 and a_1+*c* domains), which is consistent with the coarsening behavior of the domain structures with decreasing cooling rates, as shown in Figs. 2 and 4. This analysis provides quantitative insights into the cooling-rate-mediated regulation of domain size in ferroelectric thin films.

4.3 Comparison of domain structures and evolution laws between phase-field simulations and experimental observations

In this work, it should also be mentioned that a series of exotic domain structures can be stabilized by selecting appropriate cooling rate, which are consistent with experimental findings. We selected three representative configurations as examples, which are presented in Figs. 8-9. Fig. 8(a-b) compares room-temperature domain structures stabilized under a non-equibiaxial strain condition ($\varepsilon_{11} = 2.7\%, \varepsilon_{22} = 3\%$) at cooling rates of 1 K/ps and 0.01 K/ps. At the slower rate (0.01 K/ps), a threefold vertex domain emerges in Fig. 8(b), formed by the two 90° domain walls and one 180° domain wall. To better illustrate the threefold vertex domain, a magnified view of the corresponding structure in Fig. 8(b) is provided in Fig. 8(c). This simulated configuration closely matches the experimentally observed domain structures under identical strain conditions (Fig. 8(d)), where the analogous morphologies are achieved by cooling rates modulation [42].

The other two exotic domain structures formed at specific cooling rate also merit attention. We present the domain structures at cooling rates of 1 K/ps and 0.01 K/ps, under another strain condition ($\varepsilon_{11} = 2.4\%, \varepsilon_{22} = 3\%$) as shown in Fig. 9(a-b). As the cooling rates decrease to 0.01 K/ps, the domain configuration becomes significantly more ordered, accompanied by the emergence of two exotic domain structures (I and II), as highlighted in Fig. 9(b). To better illustrate these domain morphologies, magnified views are provided in Fig. 9(c-d). Fig. 9(c) shows the Type I structure from Fig. 9(b) in greater detail, where the $a_1^+ / a_1^- / a_2^+ / a_2^-$ domain variants form a flux-closure domain. This low-dimensional flux-closure domain, owing to its unique topological conservation and excellent stability, holds promise as a structural unit for

ultra-high-density information storage [44]. Fig. 9(d) shows the Type II configuration from Fig. 9(b) in greater detail, revealing a quadrupole superstructure composed of $a_1^+ / a_1^- / a_2^+ / a_2^-$ domain variants. Experimental results confirm that this structure can occur in localized regions of PTO thin films (Fig. 9(e-f)) [45]. This ordered structure can function as specialized optical gratings for metamaterials, enabling the fabrication of nanoscale optical and acoustic devices [46]. Overall, our findings propose a novel strategy for engineering exotic structures, including flux-closure domains and quadrupole superstructures, by varying the cooling rate. Notably, the feasibility of realizing flux-closure domain structures through cooling rate control has already been confirmed experimentally, supporting the validity of the proposed strategy [9].

Additionally, several results obtained in other sections of this work are also in good qualitative agreement with experimental findings. For instance, in Sections 3.1 and 3.2, we showed that a slower cooling rate promotes more ordered domain structures, consistent with experimental studies of $Pb(Zr_{0.4}Ti_{0.6})O_3$ and $BiFeO_3$ thin film systems [41]. Furthermore, in Section 4.2, we found that a lower cooling rate leads to an increase in domain size, which agrees with several experimental studies of epitaxial $PbTiO_3$ films grown on (110)-oriented $NdScO_3$ substrates [42] and $BiFeO_3$ films epitaxially grown on (001)-oriented $SrTiO_3$ substrates [43].

While our simulation results agree well with experimental observations in many respects, certain discrepancies remain, such as the findings reported for $PbZr_{0.1}Ti_{0.9}O_3$ films grown on $DyScO_3$ substrates under different cooling conditions [36]. In the experiment, the room-temperature domain structure obtained under rapid cooling shows only a few *a* domains embedded within the *c* domains, whereas slow cooling results in a noticeable increase in the *a* domain fraction. This trend differs from the simulation results shown in Fig. 2(c) in Section 3.1. The difference between the experimental and simulation results can be attributed to two main reasons: (1) the simulation assumes a constant, anisotropic compressive strain ($\varepsilon_{11} = \varepsilon_{22} = -0.2\%$), in contrast to the temperature-dependent strain in the experiment; and (2) in the simulation, the system is relaxed for a sufficient time after cooling to the target temperature,

allowing it to reach a stable state. When both the mismatch in thermal expansion coefficients between the substrate and the film , as well as the limited relaxation time are considered, our preliminary results are consistent with the key experimental observations [36], i.e., slow cooling induces *a* domains within the *c* domain matrix. However, some additional assumptions need to be introduced (i.e., thermal expansion coefficients, relaxation time), which are beyond the main assumption of the present work (constant strain upon cooling). These aspects will be investigated in future work.

4.4 Tuning the thermal conductivity of PTO thin films by misfit strains and cooling rates

For low-dimensional ferroelectric materials such as $BaTiO_3$ and $PbTiO_3$ thin films, the polarization inhomogeneity around the domain walls causes these regions to act as interfaces for phonon scattering. Specifically, the polarization gradient in the domain wall region induces local lattice distortions and polarization differences between domains, which collectively lead to phonon scattering, thereby reducing the thermal conductivity of the thin films. Therefore, variations in the fraction of domain walls and domains can significantly influence the effective thermal conductivity of PTO thin films. To investigate the effects of cooling rates on thermal conductivity, we evaluate the thermal conductivity of the obtained domain structures under different cooling rates based on effective property calculations. Fig. 10(a) shows the effect of cooling rates on the thermal conductivity under different misfit strains at room temperature. Here, the thermal conductivity (k) is obtained by $k = k^{\text{domain wall}} V_f^{\text{domain wall}} + k^{\text{domain}} V_f^{\text{domain}}$ [47], k^{domain} and $k^{\text{domain wall}}$ represent the thermal conductivities of the domains and the domain walls, respectively, while V_f^{domain} and $V_f^{\text{domain wall}}$ denote the volume fractions of the domains and the domain walls. Based on the previous study [47], it is assumed that k^{domain} is 10 times higher than $k^{\text{domain wall}}$. All calculated effective thermal conductivities (k) are normalized by k/k_0, where k_0 represents the thermal conductivity of a single-domain structure, as shown in Fig. 10(a).

The comparative analysis of the thermal conductivity mappings in Fig. 10(a) at different cooling rates reveals that slower cooling rates lead to an increase in thermal conductivity. Specifically, the region where k/k_0 is greater than 0.9 shows a significant expansion as the cooling rates decrease from quenching to 0.03 K/ps. To better quantify

the enhancement induced by slowing cooling rates, we calculate the $\Delta k/k_{\text{quench}}$ within a region of 5% misfit strains. Here can be expressed as: $\Delta k/k_{\text{quench}} = (k_{0.03\ \text{K/ps}} - k_{\text{quench}})/k_{\text{quench}} \times 100\%$, where k_{quench} and $k_{0.03\ \text{K/ps}}$ correspond to the thermal conductivity of domain structures formed under quenching and 0.03 K/ps, respectively. It can be observed that a minimum enhancement of 10% occurs in most strain regions considered in the simulation. Notably, the enhancement of thermal conductivity can reach up to 35% under a strain condition of $\varepsilon_{11} = 5\%, \varepsilon_{22} = 3\%$, which suggests an effective way to modulate the thermal conductivity of ferroelectric thin films by varying the cooling rates.

5. Conclusion

In this work, we systematically investigate the effects of cooling rates on the strain phase diagrams and equilibrium domain structures of PTO ferroelectric thin films using phase-field simulations. Our results reveal that slower cooling enhances domain regularity, increases domain width and area, and promotes the formation of flux-closure and quadrupole domain structures. Furthermore, slower cooling expands the single-phase region, significantly affecting the phase boundary position between single-phase and multiphase regions, while boundaries between two multiphase regions remain unaffected. We attribute this phenomenon to the dependence of charged domain walls density on cooling rate, as the high local electrostatic energy density at charged domain walls promotes nucleation of new domain variants. Additionally, we predict that the apparent thermal conductivity of PTO ferroelectric thin films can be significantly influenced by controlling the cooling rate, with a maximum increase of 35%. This work offers both scientific insights into the kinetic effects on phase equilibria in strained ferroelectrics and practical guidance for domain engineering in thin films. By providing a straightforward but effective strategy for accurate control of domain structures and consequently the overall functional properties, our findings have profound implications for nanodevices in electromechanical and phononic applications.

CRediT authorship contribution statement

Meng-Jun Zhou: Conceptualization, Methodology, Formal analysis, Funding

acquisition, Investigation, Project administration, Supervision, Writing–original draft, Writing–review & editing. **Peng Zhang**: Methodology, Formal analysis, Investigation, Writing–original draft, Writing–review & editing. **Bo Wang**: Conceptualization, Methodology, Formal analysis, Supervision, Writing–review & editing. **Di Yi**: Formal analysis, Supervision, Writing–review & editing. **Ce-Wen Nan**: Formal analysis, Supervision, Writing–review & editing.

Acknowledgment

This study was supported by the NSF of China (Grant No. 52102141), the open research fund of Songshan Lake Materials Laboratory (2023SLABFN10), the State Key Laboratory of New Ceramic Materials, Tsinghua University (No. KF202416), and the State Key Laboratory of Advanced Technology for Materials Synthesis and Processing (Wuhan University of Technology, 2024-KF-22). And the simulations were carried out using the Mu-PRO software suite (http://mupro.co) on the computational resources at Wuhan University of Technology. Part of this work was performed under the auspices of the U.S. Department of Energy by Lawrence Livermore National Laboratory under Contract DE-AC52-07NA27344 (B.W.).

Declaration of competing interest

No financial or personal conflicts of interest that might affect the outcomes of this research are reported by the authors.

References

[1] J. Wang et al., Epitaxial $BiFeO_3$ Multiferroic Thin Film Heterostructures, Science. 299 (2003) 1719–1722.

[2] Z. Li, X. Huang, Y. Wang, Y. Tang, X. Zhao, F. Wang, T. Wang, W. Shi, Z. Duan, Ferroelectric and piezoelectric response in (100)-oriented Mn-doped $Bi_{0.5}Na_{0.5}TiO_3$–$BaTiO_3$ thin films, J. Mater. Sci. 55 (2020) 8088–8094.

[3] L. Dai, D. Yao, F. An, M. Cheng, X. Zhong, Z. Tang, G. Zhong, Freestanding ferroelectric thin film with robust ferroelectricity via inserted dielectric layers, Mater. Today Commun. 42 (2025) 111412.

[4] P.D. Lomenzo, S. Jachalke, H. Stoecker, E. Mehner, C. Richter, T. Mikolajick, U. Schroeder, Universal Curie constant and pyroelectricity in doped ferroelectric HfO_2 thin films, Nano Energy. 74 (2020) 104733.

[5] S. Gupta, A. Paliwal, V. Gupta, M. Tomar, Ferroelectric $Sr_{0.6}Ba_{0.4}Nb_2O_6$ thin film based broadband waveguide coupled surface plasmon electro-optic modulator, Opt. Laser Technol. 122 (2020) 105880.

[6] Y. Zhang, Q. Guo, S. Zheng, X. Zhong, G. Zhong, D. Zhang, C. Ren, C. Tan, Z. Lu, Y. Zhang, Y. Tang, J. Wang, J. Yuan, Surface-step-terrace tuned second-order nonlinear optical coefficients of epitaxial ferroelectric $BaTiO_3$ films, J. Mater. Chem. C. 6 (2018) 11679–11685.

[7] B. Wang, M.J. Zhou, T. Yang, L.Q. Chen, A brief review on strain engineering of ferroelectric $K_xNa_{1-x}NbO_3$ epitaxial thin films: Insights from phase-field simulations, J. Mater. Res. 39(2024) 2918–2933.

[8] J. Yang, M. Liang, H. Yang, H. Ai, T. Zhang, Q. Han, J. Ma, H. Huang, J. Wang, Ferroelastic domain engineering in layered-perovskite Bi_2WO_6 thin films by post-annealing, J. Adv. Dielectr. 14 (2024) 2440004.

[9] S.Z. Liu, M.X. Zhu, Y.L. Tang, R.J. Jiang, W.R. Geng, Y.L. Zhu, Y.J. Wang, Y.T. Chen, T.T. Shi, X.D. Lv, J.H. Wang, S.J. Chen, X.L. Ma, Topological nanodomain engineering for multiferroic $BiFeO_3$ films via precision heat

treatment, Acta Mater. 285 (2025) 120695.

[10] V. Shelke, D. Mazumdar, G. Srinivasan, A. Kumar, S. Jesse, S. Kalinin, A. Baddorf, A. Gupta, Reduced coercive field in $BiFeO_3$ thin films through domain engineering, Adv. Mater. 23 (2011) 669–672.

[11] M.J. Zhou, B. Wang, K. Peng, H.X. Liu, L.Q. Chen, C.W. Nan, Phase-field simulation of domain size effect on dielectric and piezoelectric responses in $K_{0.5}Na_{0.5}NbO_3$ epitaxial thin films with superdomain structures, Acta Mater. 248 (2023) 118777.

[12] C. Liu, J. Wang, Strain engineering of ferroelectric negative capacitance in $PbZr_{(1-x)}Ti_xO_3$ thin films, Acta Mater. 206 (2021) 116607.

[13] S. Xu, X. Shi, H. Pan, R. Gao, J. Wang, Y. Lin, H. Huang, Strain Engineering of Energy Storage Performance in Relaxor Ferroelectric Thin Film Capacitors, Adv. Theory Simulations. 5 (2022) 2100324.

[14] H. Han, D. Kim, K. Chu, J. Park, S.Y. Nam, S. Heo, C.H. Yang, H.M. Jang, Enhanced Switchable Ferroelectric Photovoltaic Effects in Hexagonal Ferrite Thin Films via Strain Engineering, ACS Appl. Mater. Interfaces. 10 (2018) 13261-13269.

[15] L. Xu, F. Chen, F. Jin, D. Lan, L. Qu, K. Zhang, Z. Zhang, G. Gao, H. Huang, T. Li, F. Zhang, K. Wang, Z. Zhou, W. Wu, Tuning electrical properties and phase transitions through strain engineering in lead-free ferroelectric $K_{0.5}Na_{0.5}NbO_3$-$LiTaO_3$-$CaZrO_3$ thin films, Appl. Phys. Lett. 115 (2019) 202901.

[16] B. Wang, H.N. Chen, J.J. Wang, L.Q. Chen, Ferroelectric domain structures and temperature-misfit strain phase diagrams of $K_{1-x}Na_xNbO_3$ thin films: A phase-field study, Appl. Phys. Lett. 115 (2019) 092902.

[17] H. Zhang, Y.P. Feng, Y.J. Wang, Y.L. Tang, Y.L. Zhu, X.L. Ma, Strain phase diagram and physical properties of (110)-oriented $PbTiO_3$ thin films by phase-field simulations, Acta Mater. 228 (2022) 117761.

[18] M.J. Zhou, B. Wang, A. Ladera, L. Bogula, H.X. Liu, L.Q. Chen, C.W. Nan, Phase diagrams, superdomains, and superdomain walls in $K_xNa_{1-x}NbO_3$ epitaxial thin films, Acta Mater. 215 (2021) 117038.

[19] B.K. Lai, I.A. Kornev, L. Bellaiche, G.J. Salamo, Phase diagrams of epitaxial $BaTiO_3$ ultrathin films from first principles, Appl. Phys. Lett. 86 (2005) 132904.

[20] A. Grünebohm, M. Marathe, C. Ederer, Ab initio phase diagram of $BaTiO_3$ under epitaxial strain revisited, Appl. Phys. Lett. 107 (2015) 102901.

[21] J.H. Qiu, T.X. Zhao, Z.H. Chen, X.Q. Wang, N.Y. Yuan, J.N. Ding, Phase diagram and physical properties of (110) oriented $Ba(Zr_{0.08}Ti_{0.92})O_3$ thin film, Solid State Commun. 289 (2019) 1–4.

[22] D. V. Karpinsky, E.A. Eliseev, F. Xue, M. V. Silibin, A. Franz, M.D. Glinchuk, I.O. Troyanchuk, S.A. Gavrilov, V. Gopalan, L.Q. Chen, A.N. Morozovska, Thermodynamic potential and phase diagram for multiferroic bismuth ferrite ($BiFeO_3$), Npj Comput. Mater. 3 (2017) 20.

[23] Y.G. Lu, S.F. Deng, L.J. Gong, J.T. Yang, Effect of external stress on phase diagrams and dielectric properties of epitaxial ferroelectric thin films grown on orthorhombic substrates, Trans. Nonferrous Met. Soc. China. 16 (2006) 912–916.

[24] W.S. Yan, R. Zhang, X.Q. Xiu, Z.L. Xie, P. Han, R.L. Jiang, S.L. Gu, Y. Shi, Y.D. Zheng, Impact of lattice strain on the phase formation, polarization, and dielectric constant of $PbZr_{1-x}Ti_xO_3$ films, Appl. Phys. Lett. 92 (2008) 064103.

[25] V.G. Kukhar, N.A. Pertsev, H. Kohlstedt, R. Waser, Polarization states of polydomain epitaxial $Pb(Zr_{1-x}Ti_x)O_3$ thin films and their dielectric properties, Phys. Rev. B. 73 (2006) 214103.

[26] N.A. Pertsev, V.G. Koukhar, Polarization instability in polydomain ferroelectric epitaxial thin films and the formation of heterophase structures, Phys. Rev. Lett. 84 (2000) 3722–3725.

[27] S.P. Alpay, A.L. Roytburd, Thermodynamics of polydomain heterostructures. III. Domain stability map, J. Appl. Phys. 83 (1998) 4714–4723.

[28] B. Wang, L.Q. Chen, Theory of strain phase equilibria and diagrams, Acta Mater. 274 (2024) 120025.

[29] B. Wang, M.J. Zhou, A. Ladera, L.Q. Chen, Strain phase equilibria and phase-field method of ferroelectric polydomain: A case study of monoclinic $K_xNa_{1-x}NbO_3$ thin films, J. Am. Ceram. Soc. 107 (2024) 7692–7710.

[30] G. Sheng, J.X. Zhang, Y.L. Li, S. Choudhury, Q.X. Jia, Z.K. Liu, L.Q. Chen, Domain stability of $PbTiO_3$ thin films under anisotropic misfit strains: Phase-field simulations, J. Appl. Phys. 104 (2008) 054105.

[31] X.W. Guo, Y.J. Wang, H. Zhang, Y.L. Tang, Y.L. Zhu, X.L. Ma, Misfit strain-temperature phase diagram of multi-domain structures in (111)-oriented ferroelectric $PbTiO_3$ films, Acta Mater. 196 (2020) 539–548.

[32] L. Feigl, P. Yudin, I. Stolichnov, T. Sluka, K. Shapovalov, M. Mtebwa, C.S. Sandu, X.K. Wei, A.K. Tagantsev, N. Setter, Controlled stripes of ultrafine ferroelectric domains, Nat. Commun. 5 (2014) 4677.

[33] X. Wu, G. Wang, D. Zeng, Prediction of the glass forming ability in a Fe-25%B binary amorphous alloy based on phase-field method, J. Non. Cryst. Solids. 466–467 (2017) 52–57.

[34] Y. Yin, B.H. Luo, Z.H. Bai, H.B. Jing, Quench sensitivity of Al–Cu–Mg alloy thick plate, Rare Met. 42 (2023) 3161–3169.

[35] L.Q. Chen, Phase-field method of phase transitions/domain structures in ferroelectric thin films: A review, J. Am. Ceram. Soc. 91 (2008) 1835–1844.

[36] L. Feigl, P.E. Janolin, T. Yamada, M. Iwanowska, C.S. Sandu, N. Setter, Post-deposition control of ferroelastic stripe domains and internal electric field by thermal treatment, Appl. Phys. Lett. 106 (2015) 032902.

[37] L. Van Lich, V.H. Dinh, Formation of polarization needle-like domain and its unusual switching in compositionally graded ferroelectric thin films: an improved phase field model, RSC Adv. 9 (2019) 7575–7586.

[38] A.R. Damodaran, S. Pandya, J.C. Agar, Y. Cao, R.K. Vasudevan, R. Xu, S. Saremi, Q. Li, J. Kim, M.R. McCarter, L.R. Dedon, T. Angsten, N. Balke, S. Jesse, M. Asta, S. V. Kalinin, L.W. Martin, Three-State Ferroelastic Switching and Large Electromechanical Responses in $PbTiO_3$ Thin Films, Adv. Mater. 29 (2017) 1702069.

[39] Y.L. Li, S.Y. Hu, S. Choudhury, M.I. Baskes, A. Saxena, T. Lookman, Q.X. Jia, D.G. Schlom, L.Q. Chen, Influence of interfacial dislocations on hysteresis loops of ferroelectric films, J. Appl. Phys. 104 (2008) 104110.

[40] Y.L. Li, S.Y. Hu, Z.K. Liu, L.Q. Chen, Effect of substrate constraint on the stability and evolution of ferroelectric domain structures in thin film, Acta Mater. 50 (2002) 395–411.

[41] Y. Nahas, S. Prokhorenko, J. Fischer, B. Xu, C. Carrétéro, S. Prosandeev, M. Bibes, S. Fusil, B. Dkhil, V. Garcia, L. Bellaiche, Inverse transition of labyrinthine domain patterns in ferroelectric thin films, Nature 577 (2020) 47–51.

[42] J. Ma, Y. Zhu, Y. Tang, M. Han, Y. Wang, N. Zhang, M. Zou, Y. Feng, W. Geng, X. Ma, Modulation of charged a_1/a_2 domains and piezoresponses of tensile strained $PbTiO_3$ films by the cooling rate, RSC Adv. 9 (2019) 13981–13990.

[43] M. Liang, J. Yang, H. Yang, C. Liang, Z. Nie, H. Ai, T. Zhang, J. Ma, H. Huang, J. Wang, Effect of annealing conditions on surface morphology and ferroelectric domain structures of $BiFeO_3$ thin films, J. Adv. Dielectr. 14 (2024) 2440002.

[44] Y.L. Tang, Y.L. Zhu, X.L. Ma, A.Y. Borisevich, A.N. Morozovska, E.A. Eliseev, W.Y. Wang, Y.J. Wang, Y.B. Xu, Z.D. Zhang, S.J. Pennycook, Observation of a periodic array of flux-closure quadrants in strained ferroelectric $PbTiO_3$ films, Science. 348 (2015) 547–551.

[45] F. Borodavka, I. Gregora, A. Bartasyte, S. Margueron, V. Plausinaitiene, A. Abrutis, J. Hlinka, Ferroelectric nanodomains in epitaxial $PbTiO_3$ films grown on $SmScO_3$ and $TbScO_3$ substrates, J. Appl. Phys. 113 (2013) 187216.Z.

[46] Z. Liu, X. Zhou, B. Feng, B.X. Xu, Engineered periodic quadrupole superstructure in ferroelectric thin films via flexoelectricity, Acta Mater. 216 (2021) 117126.

[47] E. Langenberg, D. Saha, M.E. Holtz, J.J. Wang, D. Bugallo, E. Ferreiro-Vila, H. Paik, I. Hanke, S. Ganschow, D.A. Muller, L.Q. Chen, G. Catalan, N. Domingo, J. Malen, D.G. Schlom, F. Rivadulla, Ferroelectric Domain Walls in $PbTiO_3$ Are Effective Regulators of Heat Flow at Room Temperature, Nano Lett. 19 (2019) 7901–7907.

Figure and captions

Fig. 1

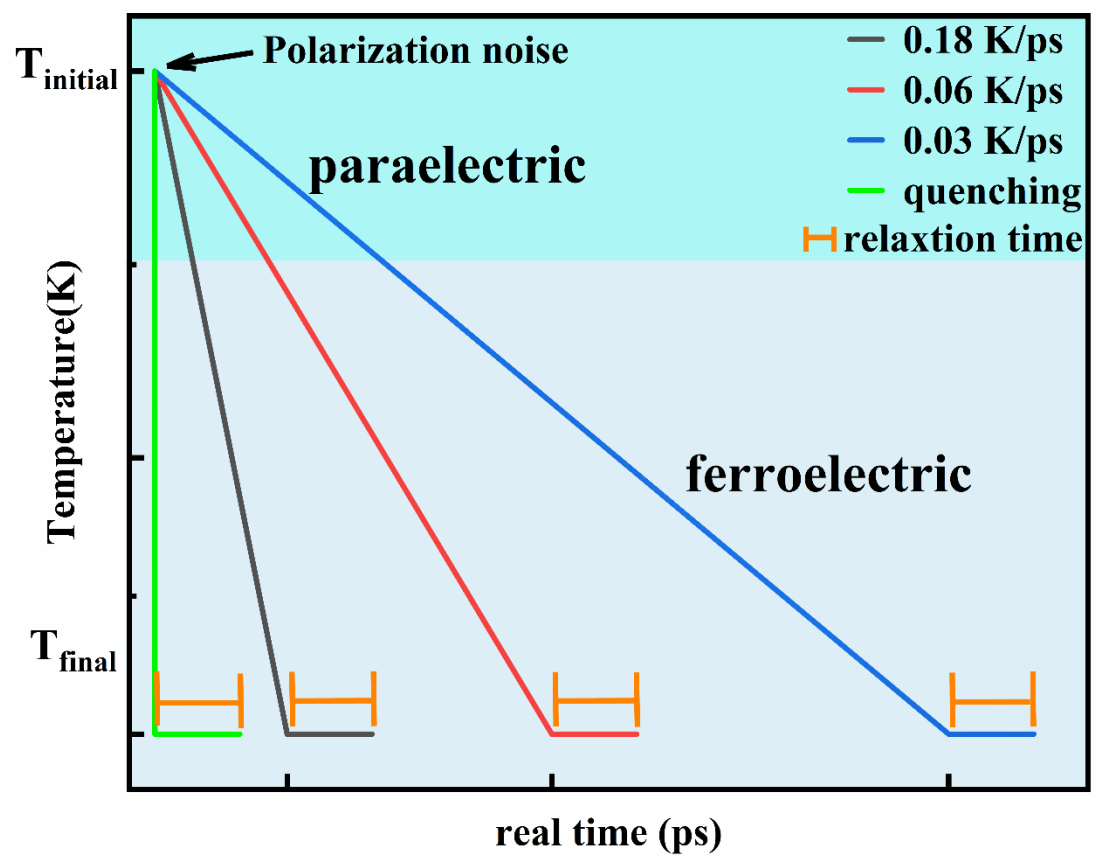

Fig. 1 Schematic illustration of four cooling cases: quenching, 0.18 K/ps, 0.06 K/ps, and 0.03 K/ps.

Fig. 2

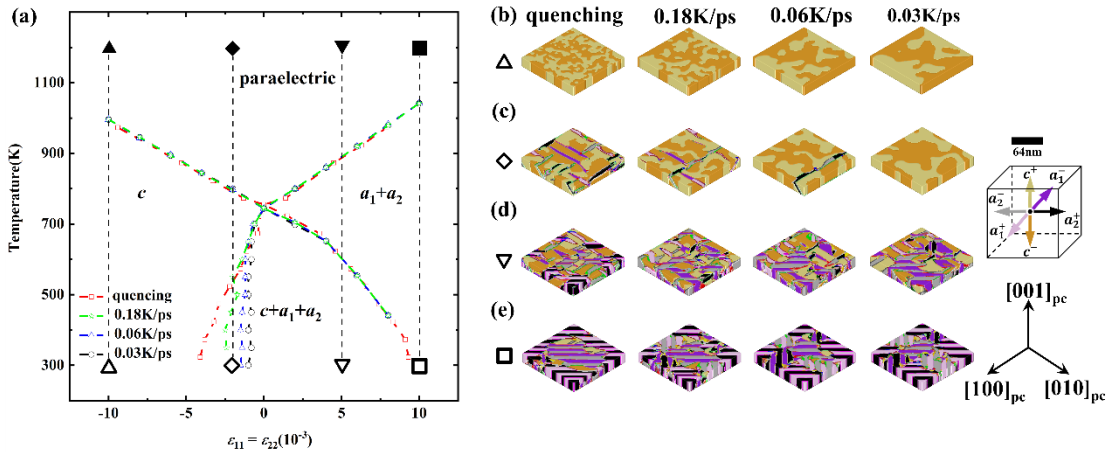

Fig. 2 The temperature-misfit strain phase diagrams of (001)-oriented PTO thin films and the typical domain structures at different cooling rates. (a) The temperature-misfit strain phase diagrams at different cooling rates. (b-e) Room-temperature domain structures under different isotropic misfit strains and cooling rates. (b) $\varepsilon_{11}=\varepsilon_{22}=-1\%$; (c) $\varepsilon_{11}=\varepsilon_{22}=-0.2\%$; (d) $\varepsilon_{11}=\varepsilon_{22}=0.5\%$; (e) $\varepsilon_{11}=\varepsilon_{22}=1\%$. The configurations are shaded according to the orientation of the polar vectors, as indicated on the right.

Fig. 3

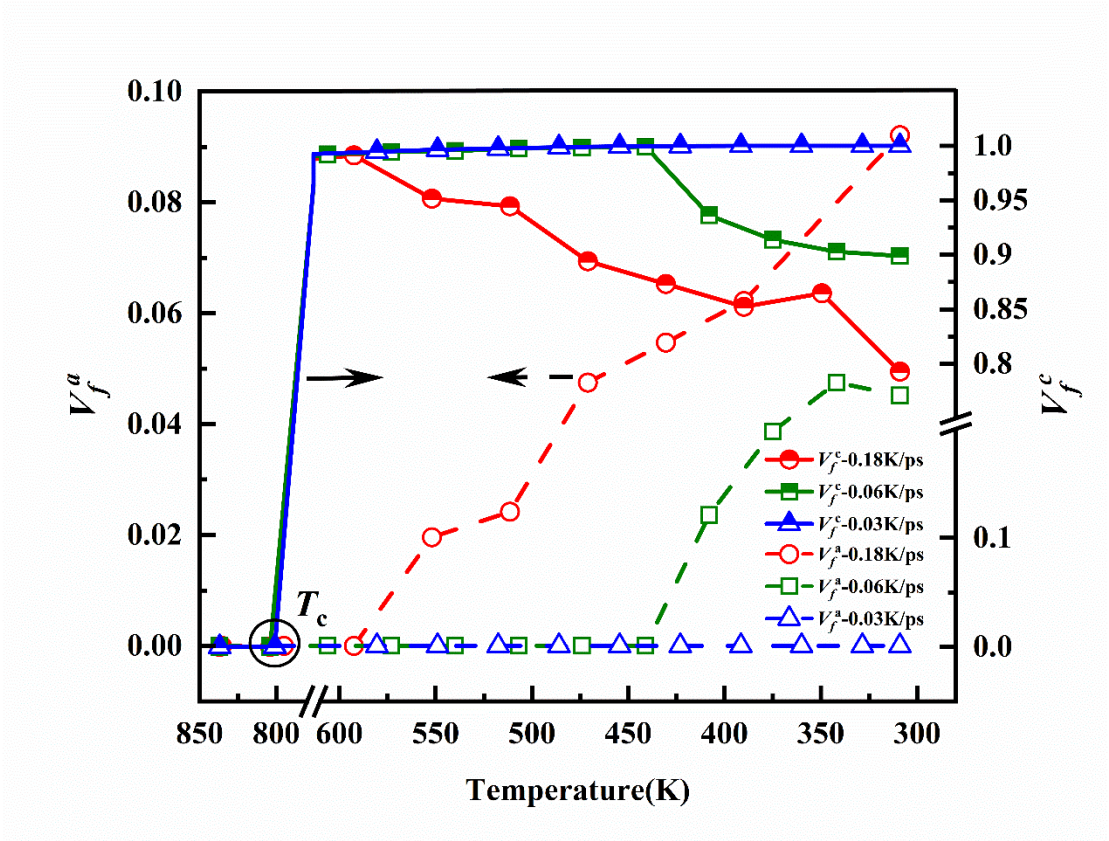

Fig. 3 The curves of V_f^a and V_f^c as a function of temperature at different cooling rates with $\varepsilon_{11} = \varepsilon_{22} = -0.2\%$. The curves for different cooling rates and phases are plotted as different symbols and lines, with symbols and lines in red, green, and blue representing cooling rates from fast (0.18 K/ps) to slow (0.03 K/ps), respectively, as shown in the lower-right corner of the figure.

Fig. 4

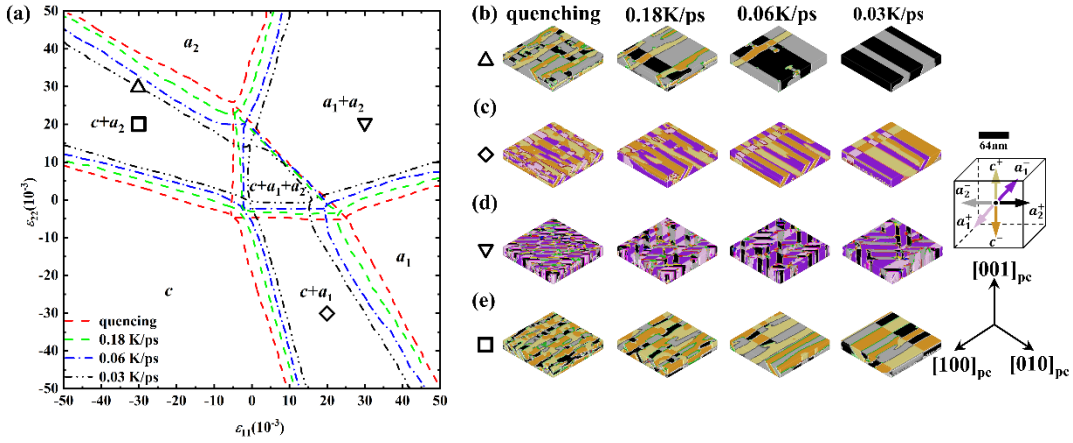

Fig. 4 The misfit strain-misfit strain phase diagrams of (001)-oriented PTO thin films and the typical domain structures. (a) The room-temperature misfit strain-misfit strain phase diagrams under four different cooling rates. (b-e) Room-temperature domain configurations under different anisotropic misfit strains and cooling rates. (b) $\varepsilon_{11}=-3\%,\varepsilon_{22}=3\%$; (c) $\varepsilon_{11}=2\%,\varepsilon_{22}=-3\%$; (d) $\varepsilon_{11}=3\%,\varepsilon_{22}=2\%$; (e) $\varepsilon_{11}=-3\%,\varepsilon_{22}=2\%$. The domains are shaded according to the orientation of the polar vectors, as indicated on the right.

Fig. 5

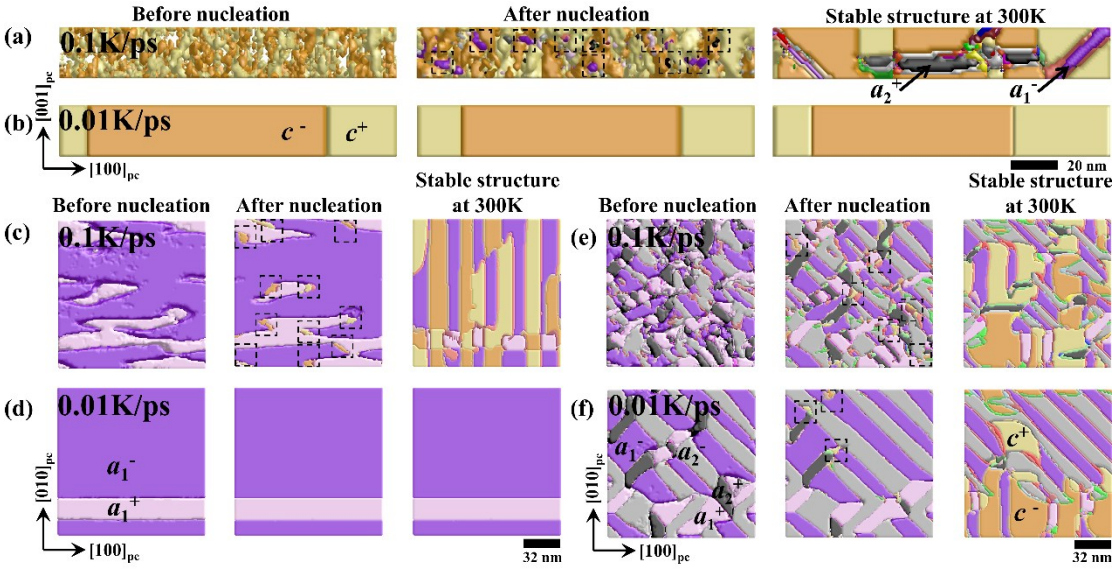

Fig. 5 The evolution of initial domain structures dominated by polarization noise under varying strain conditions and cooling rates. 'Before nucleation', 'After nucleation', and 'Stable structure at 300K' represent the domain morphologies before nucleation, after nucleation, and the equilibrium state at room temperature, respectively. The cooling rates are marked in the figures, such as 0.1 K/ps and 0.01 K/ps. (a-b) $\varepsilon_{11} = \varepsilon_{22} = -0.2\%$. (c-d) $\varepsilon_{11} = 3\%, \varepsilon_{22} = -3\%$. (e-f) $\varepsilon_{11} = \varepsilon_{22} = 0.5\%$. The dashed squares in (a), (c), (e), and (f) highlight preferential nucleation sites, where subsequent domain growth is localized.

Fig. 6

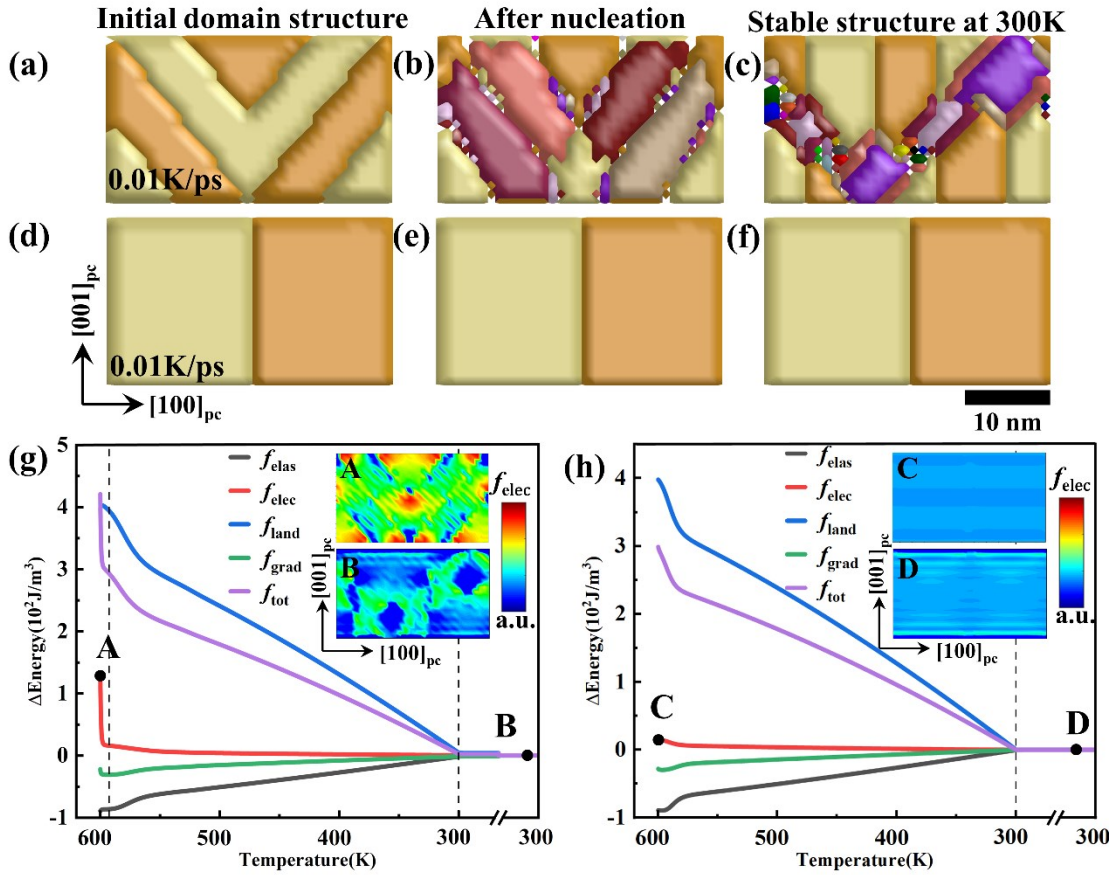

Fig. 6 The evolution of two types of preset *c* domain structures and corresponding energy density variations under biaxial strain conditions ($\varepsilon_{11} = \varepsilon_{22} = -0.2\%$) during cooling at 0.1 K/ps. (a-c) The evolution of the preset *c* domain structure with charged domain walls. (d–f) The evolution of the preset *c* domain structure without charged domain walls. Three stages are shown: (1) Initial domain structure (artificially preset domain structure), (2) After nucleation (post-nucleation morphology), and (3) Stable structure at 300K (equilibrium domain structure at room temperature). (g-h) Corresponding energy density variations for (a-c) and (d-f). The insets in (g-h) are the electrostatic energy density distributions at selected states.

Fig. 7

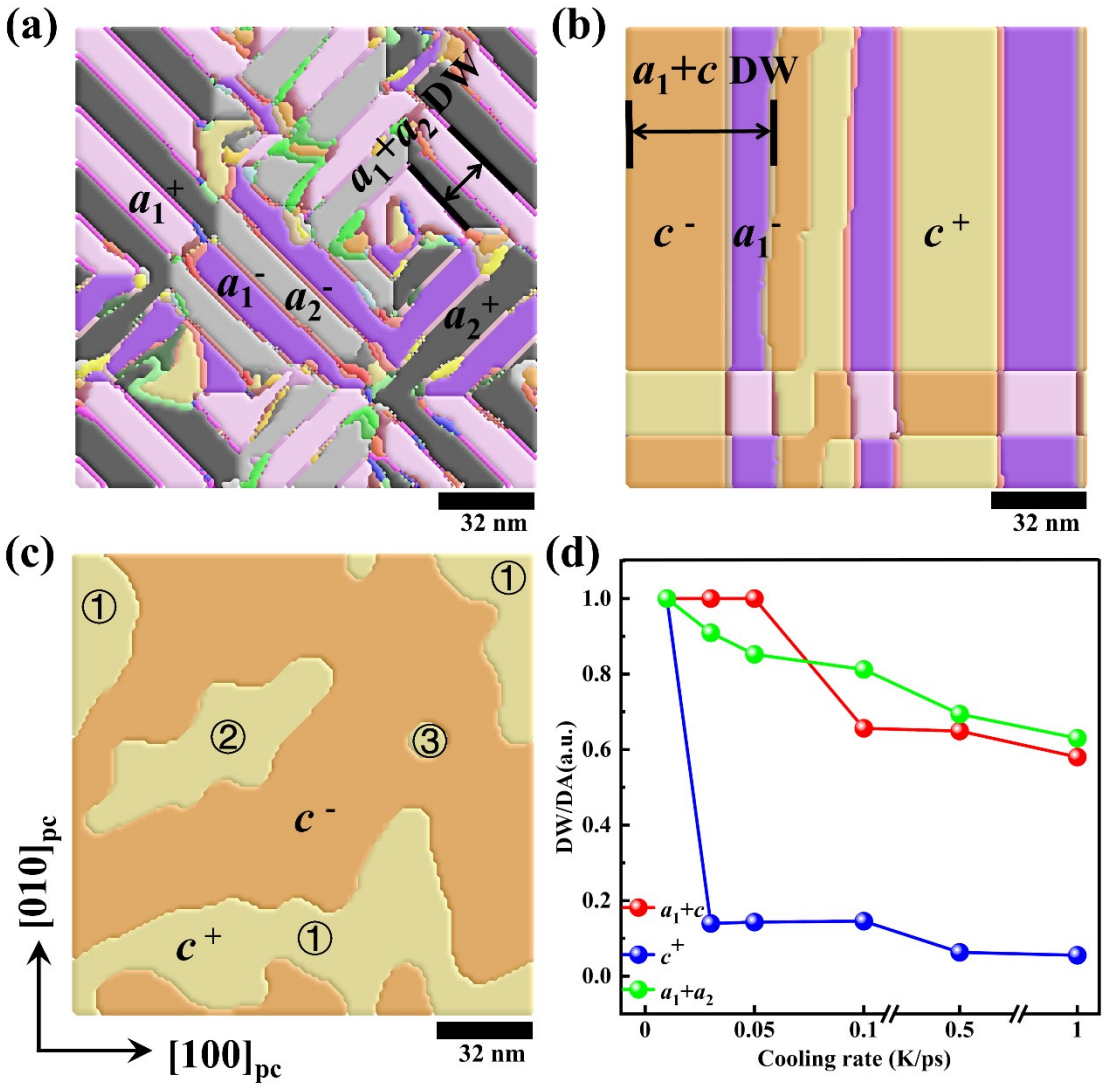

Fig. 7 The cooling rate dependence of domain size for three representative domain structures. (a-c) The plan-view images of representative domain structures: (a) a_1+a_2 domains under $\varepsilon_{11} = \varepsilon_{22} = 1\%$. (b) a_1+c domains under $\varepsilon_{11} = 2\%, \varepsilon_{22} = -3\%$. (c) c domains under $\varepsilon_{11} = \varepsilon_{22} = -1\%$. (d) The correlation between domain size (DW and DA) and cooling rates (0.01-1 K/ps). Domain size is quantified by the domain width (DW) of a_1+a_2 and a_1+c domains (green and red circles) and the average domain area (DA) of c^+ domains (bule circles).

Fig. 8

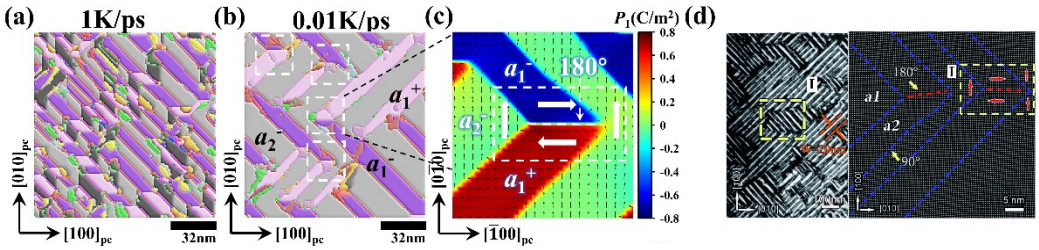

Fig. 8 The comparison of threefold vertex domain between phase-field simulations and experimental observations. (a-b) The simulated domain configurations after cooling at 1 K/ps (a) and 0.01 K/ps (b) under $\varepsilon_{11} = 2.7\%, \varepsilon_{22} = 3\%$. The dashed squares in (b) represent the threefold vertex domain. (c) The local polarization distribution within one of the dashed squares in (b). (d) The experimentally observed threefold vertex domain and its local polarization mapping. Fig. 8(d) reprinted with permission [39]. Copyright 2019 Royal Society of Chemistry Publishing.

Fig. 9

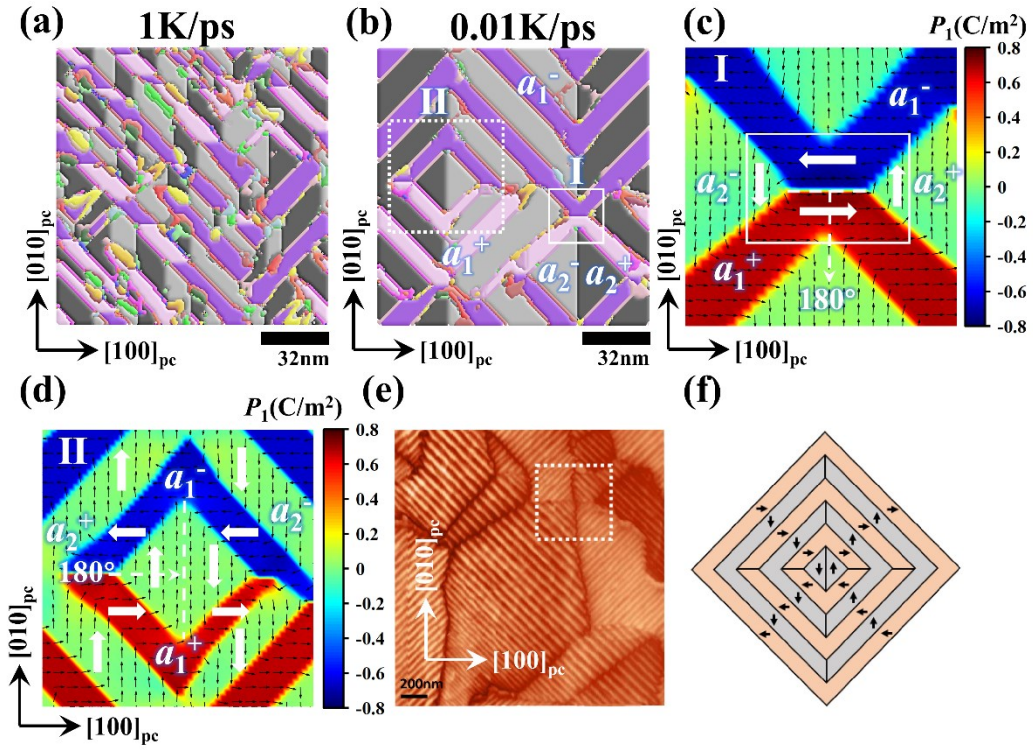

Fig. 9 The comparison of flux-closure domain and quadrupole superstructure between phase-field simulations and experimental observations. (a-b) The simulated domain configurations after cooling at 1 K/ps (a) and 0.01 K/ps (b) under $\varepsilon_{11} = 2.4\%, \varepsilon_{22} = 3\%$, with exotic configurations labeled as I (flux-closure) and II (quadrupole) in (b). (c) The magnified view of the region I (solid square) in (b), showing a flux-closure domain composed of $a_1^+ / a_1^- / a_2^+ / a_2^-$ domain variants. (d) The enlarged view of region II (dashed square) in (b), revealing a quadrupole superstructure with $a_1^+ / a_1^- / a_2^+ / a_2^-$ domain variants. (e-f) The experimentally observed quadrupole superstructure (dashed regions) in PTO thin films and corresponding polarization arrangements. Fig. 9(e-f) reprinted with permission [41]. Copyright 2013 AIP Publishing.

Fig. 10

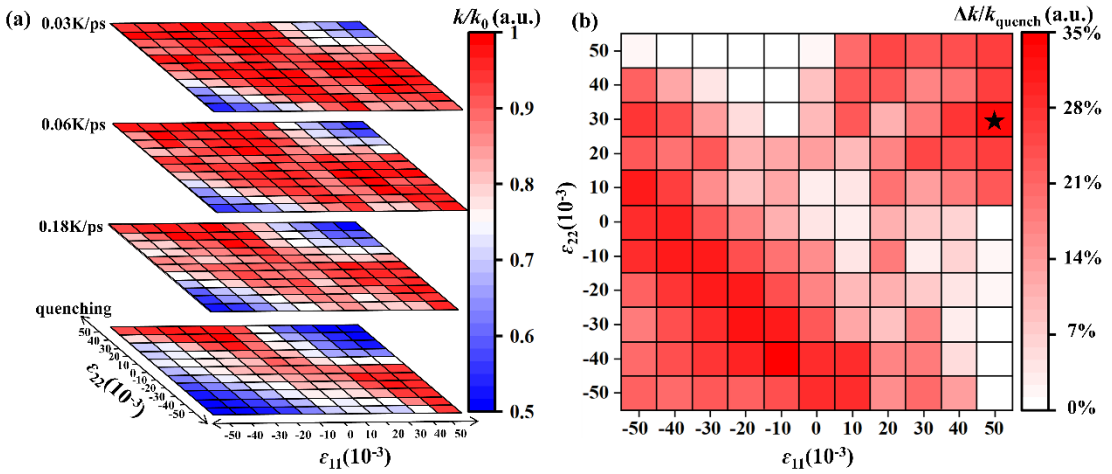

Fig. 10 The room-temperature thermal conductivity mappings and enhancement in PTO thin films under different cooling rates. (a) The thermal conductivity mappings for four cooling conditions: quenching, 0.18 K/ps, 0.06 K/ps, and 0.03 K/ps. (b) The mapping of the thermal conductivity enhancement (relative to quenching), the maximum value is marked by '★'. ($\Delta k = k_{0.03\ \mathrm{K/ps}} - k_{\mathrm{quench}}$)